Construction and Building Materials 406 (2023) 132730

Contents lists available at ScienceDirect

Construction and Building Materials

journal homepage: www.elsevier.com/locate/conbuildmat

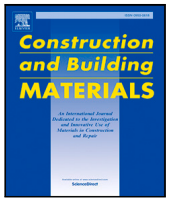

Uncertainty quantification in timber-like beams using sparse grids: Theory and examples with off-the-shelf software utilization

Giuseppe Balduzzi [a], Francesca Bonizzoni [b,*], Lorenzo Tamellini [c]

[a] DICAr - Department of Civil Engineering and Architecture, University of Pavia, Via Ferrata, 3, Pavia, 27100, Italy
[b] MOX - Dipartimento di Matematica, Politecnico di Milano, Piazza Leonardo da Vinci, 32, Milano, 20133, Italy
[c] IMATI - Istituto di Matematica Applicata e Tecnologie Informatiche "E. Magenes", Consiglio Nazionale delle Ricerche, Via Ferrata, 5a, Pavia, 27100, Italy

ARTICLE INFO

Keywords:
Timber structures
Variable mechanical properties
Uncertainty quantification
Stochastic collocation method
Sparse grids
Isogeometric collocation

ABSTRACT

When dealing with timber structures, the characteristic strength and stiffness of the material are made highly variable and uncertain by the unavoidable, yet hardly predictable, presence of knots and other defects. In this work, we apply the sparse grids stochastic collocation method to perform uncertainty quantification for structural engineering in the scenario described above. Sparse grids have been developed by the mathematical community in the last decades, and their theoretical background has been rigorously and extensively studied. The document proposes a brief practice-oriented introduction with minimal theoretical background, provides detailed instructions for the use of the off-the-shelf Sparse Grid Matlab kit (freely available online and straightforward to use) and discusses two preliminary examples inspired from timber engineering problems that highlight how sparse grids exhibit superior performances compared to the plain Monte Carlo method.

1. Introduction

Timber is one of the oldest building materials. Used since the prehistory, wood has been employed in all ages and by all civilizations, often with peculiar technologies [1]. Between the Nineteenth and Twentieth centuries other materials (like cast iron, steel, aluminium, and concrete) became largely available, deeply impacting word economic development and sustaining human expansion [2]. In recent years, climate change emerged as a new, urgent problem and construction and related industries (in particular, concrete and steel ones) are the ones with greatest environmental impact [3,4]. In this context, timber and wood-based structural elements are experiencing a new springtime. Indeed, despite several aspects like durability, moisture sensitivity and fire resistance need ad-hoc treatments [5–7], wood presents extremely high strength vs weight ratio, low heat conductivity [8] and it is a renewable resource (if forests and production processes are properly managed) [9]. Furthermore, photosynthesis traps a significant amount of carbon dioxide ($\approx$ 50% of dry wood is constituted by carbon) that remains within wood for its whole life [10]. As a consequence, it represents the best candidate for replacing materials with more significant environmental impact.

However, the main problem that needs to be addressed is the huge variability and uncertainty in the mechanical properties of wood, consequence of the natural growth and sawing of logs: [8] specifies that the strength of wood specimens can change by an order of magnitude, even within the same wood species. In particular, knots – resulting from the insertion of branches in the stem – often coincide with the point where cracks start, therefore representing the weak point of structural elements [11]. Such a situation does not allow for an economically convenient exploitation of the material, and several strategies have been developed to limit the negative influence of defects on the performance of the structural element. The oldest is represented by grading, which consists in different procedures and technologies aiming at sorting sawn timber (and boards used for the manufacturing of glued laminated timber beams and cross laminated timber plates) in classes with assigned characteristic strength [8, Article B5]. Nowadays, novel technologies – like laser scanners [12] and X-ray computer tomography [13] – allow for the detection of grain direction and wood density, which have been employed for the reconstruction of knot geometry and the estimation of the mechanical properties of the wood [14,15]. However, the evaluation of mechanical behavior of wood is characterized by high levels of uncertainty, despite the continuous development of analysis and manufacturing technologies: a quantitative assessment of how the uncertainty on the mechanical behavior of wood translates to uncertainty on the structural behavior of timber construction can be done by means of Uncertainty Quantification (UQ) techniques.

* Corresponding author.
E-mail addresses: giuseppe.balduzzi@unipv.it (G. Balduzzi), francesca.bonizzoni@polimi.it (F. Bonizzoni), tamellini@imati.cnr.it (L. Tamellini).

https://doi.org/10.1016/j.conbuildmat.2023.132730
Received 12 December 2022; Received in revised form 19 May 2023; Accepted 31 July 2023

UQ techniques applied to timber and other building materials, such as masonry and reinforced concrete, as well as other problems of interest to practitioners [16,17] have been object of preliminary investigations in the recent engineering literature by a multitude of approaches ranging from standard sampling methods as in [18,19] to more advanced methods such as Latin hypercube sampling [20], Stochastic Galerkin [21,22], the method of moment equations [23], Gaussian Processes [24] and machine learning [25,26]. However, UQ approaches as discussed in the engineering literature are usually targeted at specific engineering problems. Furthermore, they often propose imprecise treatments of the mathematical aspects of the problem (like, e.g., error estimates and convergence rates), typically preventing the immediate comparison with other available methods and, ultimately, the choice of the most performing one. On the contrary, mathematicians have been developing the above-mentioned and several other methods as general-purpose tools, providing also detailed theoretical results; in particular, see e.g., [27,28] for a general introduction to stochastic Galerkin, [29–32] for the method of moment equations, and [33] for Gaussian Processes. Unfortunately, such methods are often complex to be implemented and might not be available as ready-to-use software, discouraging practitioners from their use.

The present contribution deals with the numerical discretization of the equilibrium equations under uncertainty for a timber-like planar body: more precisely, we assume that its elasticity modulus depends on a set of parameters modeling the random location and shape of knots under the simplistic assumptions of heterogeneous and isotropic material. As a result, the displacement vector depends on both the space variable and the set of parameters. The equations – along the space variable – are discretized following the isogeometric analysis (IGA) principles, specifically the IGA collocation that combines high-performance with easy implementation, thanks to the possibility of directly using the strong formulation of the problem. The parametric dependence is treated using the stochastic collocation method based on Smolyak sparse grids, an efficient UQ technique proposed and deeply analyzed by the mathematical community during the latest decades [34,35] and implemented in several packages like e.g., the Sparse Grid Matlab kit [36]. The sparse grids methodology is most effective when the problem at hand depends on a moderate number of uncertain parameters (say up to 20/30 parameters, although applications to problems with hundreds of random variables are available in the literature [37,38]), and the outputs of the model depend smoothly on the input parameters.

The main contributions of the present work are: (i) the superiority of the stochastic collocation method with respect to the plain Monte Carlo method is demonstrated by means of several numerical tests in the continuum mechanics framework; (ii) algorithmic and implementation details are provided to show its ease of use and possible application to any structural engineering problem. Timber structure industry may take advantage of the method in order to perform a more accurate and reliable analysis of structural performance of timber elements as well as to achieve a more efficient use of raw materials. Similarly, practitioners can benefit from the presented tools during monitoring, restoration, and maintenance of new or existing structures, where the randomness of material properties often plays a central role.

The rest of the paper is organized as follows. In Section 2 we introduce the problem of interest, namely the elasticity equation for timber-like beams, where the material variability is encoded in a set a parameters; moreover, Section 2.2 details the numerical scheme applied to discretize the model problem in the physical variable. Section 3 is dedicated to the UQ methodology that we employ throughout the work. In Section 4 a forward UQ analysis is performed on two numerical experiments, namely, the expectation and the probability density function of selected quantities of interest are computed and the global sensitivity analysis is carried out. The conclusions are drawn in Section 5.

2. Deterministic mechanical problem

2.1. Continuum mechanic PDEs

Let $D = [0, L] \times [0, H] \subset \mathbb{R}^2$ denote a two-dimensional timber beam with length $L > 0$ and height $H > 0$. Let $\mathbb{C}$ denote the fourth order stiffness tensor, which is assumed to depend on the space variable $(x, y) \in D$ as well as on a set of N parameters $\boldsymbol{p} = (p_1, \dots, p_N)$ randomly varying in the hyperrectangle $\Gamma := \Gamma_1 \times \cdots \times \Gamma_N \subset \mathbb{R}^N$, with $\Gamma_n = [a_n, b_n] \subset \mathbb{R}$ for all $n = 1, \dots, N$. In particular, $\mathbb{C}$ assumes the following form:

$$\mathbb{C}(x, y, \boldsymbol{p}) = \begin{bmatrix} E(x, y, \boldsymbol{p}) & 0 & 0 \\ 0 & E(x, y, \boldsymbol{p}) & 0 \\ 0 & 0 & \frac{E(x,y,\boldsymbol{p})}{2} \end{bmatrix}, \tag{1}$$

where the (positive) parameter-dependent elasticity modulus $E(x, y, \boldsymbol{p})$ is modeled as

$$E(x, y, \boldsymbol{p}) = E_0\, \alpha(x, y, \boldsymbol{p}). \tag{2}$$

Specific information on the value assumed by $E_0 \in \mathbb{R}_+$ as well as the form of the function $\alpha(x, y, \boldsymbol{p}) : D \to \mathbb{R}_+$ will be provided in Section 4.

Given a parameter-independent external load $\boldsymbol{t} = (t_x, t_y)$, we look for the displacement $\boldsymbol{u} = (u_x, u_y) : D \times \Gamma \to \mathbb{R}^2$ such that

$$\begin{cases} \operatorname{div}(\mathbb{C}(x, y, \boldsymbol{p}) : \nabla^s \boldsymbol{u}(x, y, \boldsymbol{p})) = \boldsymbol{0}, & (x, y) \in D, \\ (\mathbb{C}(x, y, \boldsymbol{p}) : \nabla^s \boldsymbol{u}(x, y, \boldsymbol{p})) \cdot \boldsymbol{n} = \boldsymbol{t}(x, y), & (x, y) \in \Sigma_t, \\ \boldsymbol{u}(x, y, \boldsymbol{p}) = \boldsymbol{0}, & (x, y) \in \Sigma_s, \end{cases} \tag{3}$$

where $\{\Sigma_t, \Sigma_s\}$ is a partition of ∂D and ∇^s denotes the symmetric gradient. The differential operators in (3) are intended with respect to the physical variables x, y. Note that, in the present paper, the beam material is assumed heterogeneous (since the stiffness tensor depends on x, y) and isotropic. The latter assumption is not fulfilled in the specific case of timber beams. However, it simplifies the theoretical and numerical treatment of the problem addressed. The generalization of the presented results to the anisotropic framework is worth investigating and will be addressed in a future contribution.

2.2. IGA discretization in the space variables

Using the notation on provided in Appendix A, we look for approximations to u_x, u_y of the form

$$u_x(x, y) \approx \sum_{i=1}^{N_{coll}} \sum_{j=1}^{M_{coll}} (\hat{u_x})_{i,j} R_{i,j}^{r,q}(x, y)$$
$$u_y(x, y) \approx \sum_{i=1}^{N_{coll}} \sum_{j=1}^{M_{coll}} (\hat{u_y})_{i,j} R_{i,j}^{r,q}(x, y)$$

where $R_{i,j}^{r,q}(x, y)$ are bi-variate B-splines, and we require them to be strong solutions to Eq. (3).

The obtained equations are then collocated at the Greville abscissae $(\hat{x}_i, \hat{y}_j)$ $(i = 1, \dots, N_{coll} - 1,\ j = 1, \dots, M_{coll} - 1)$, which can be computed as:

$$\begin{aligned} \hat{x}_i &= \frac{x_{i+2} + x_{i+3} + \cdots + x_{i+r}}{r - 1}, \quad i = 1, \dots, N_{coll} - 1, \\ \hat{y}_j &= \frac{y_{j+2} + y_{j+3} + \cdots + y_{j+q}}{q - 1}, \quad j = 1, \dots, M_{coll} - 1. \end{aligned} \tag{4}$$

The resulting algebraic system of equations, consisting of $2\left(N_{coll} - 1\right)\left(M_{coll} - 1\right)$ equations in the $2N_{coll}M_{coll}$ unknowns (i.e., $N_{coll} \times M_{coll}$ unknowns for both u_x and u_y), must be finally completed by $2N_{coll} + 2M_{coll} - 2$ suitable boundary conditions to be imposed as additional equations, as specified in [39].

3. Sparse grids and Uncertainty Quantification

3.1. A surrogate-modeling approach to Uncertainty Quantification

As discussed in Section 2, the beam model depends on N uncertain parameters, collected in the vector $\boldsymbol{p} \in \Gamma$. More precisely, we assume that each component p_n is a uniform random variable that can take values in the range Γ_n (we write $p_n \sim \mathcal{U}(\Gamma_n)$); we further assume that all random variables are independent, so that the probability density function (pdf) of $\boldsymbol{p}$ is simply the constant function $\rho(\boldsymbol{p}) = \prod_{n=1}^{N} \frac{1}{b_n - a_n}$.

The choice of using uniformly distributed independent random variables has been made for the sake of simplicity. Notice that it is not that restrictive. Indeed, in the general case when p_i are non-independent and/or non-uniform random variables, one could always introduce a non-linear map Θ such that $z_i = \Theta(p_i)$ with z_i uniform random variables, following the well-known theory of copulas, see [40].

Let us moreover denote by $f \in \mathbb{R}$ the quantity of interest (QoI) or output of the beam equation (which we will call hereafter Full-Order Model, FOM), e.g., the displacement or the strain in a point of the beam. f can then be seen as a N-variate function of the uncertain parameters, $f = f(\boldsymbol{p}), f : \Gamma \to \mathbb{R}$ (generalizations to vector-valued quantities of interest, i.e., $f : \Gamma \to \mathbb{R}^P$, is straightforward; one such example is when we consider the entire displacement field as QoI).

In this setup, we are interested in "quantifying the uncertainties" of the QoI due to the variability of $\boldsymbol{p}$; to this end, we would like to compute statistical indices for $f(\boldsymbol{p})$ such as its expected value and variance

$$\mathbb{E}[f] = \int_{\Gamma} f(\boldsymbol{p})\rho(\boldsymbol{p})d\boldsymbol{p}, \tag{5}$$
$$\mathbb{V}[f] = \int_{\Gamma} (f(\boldsymbol{p}) - \mathbb{E}[f])^2 \rho(\boldsymbol{p})d\boldsymbol{p} = \mathbb{E}[f^2] - \mathbb{E}[f]^2,$$

as well as higher order indices (such as kurtosis and skewness), and ideally its pdf. This task is usually called UQ.

A successful approach to perform UQ is to build a so-called surrogate model for the QoI, following an offline/online paradigm. More precisely, in a preliminary offline phase, a number of beam problems is solved, for certain judiciously selected combinations of values of $\boldsymbol{p}$, and the corresponding values of $f(\boldsymbol{p})$ stored; a so-called surrogate model is then constructed out of these values (by e.g., interpolation or least-squares regression). During the subsequent online phase, quantities such as those in Eq. (5) are efficiently computed by evaluating the surrogate model (a cheap operation that essentially involves evaluating a polynomial expression) instead of repeatedly solving the beam problem. In the following, we construct a so-called *sparse grids surrogate model*, but many other methods for building surrogate models are available in literature (e.g., Polynomial Chaos, Reduced Basis, Gaussian Processes, Radial Basis Functions, Neural Networks, just to name a few — we refer e.g., to [41] for an overview). In the context of timber engineering, surrogate models have also been employed in [42].

3.2. Mathematical description of sparse grids

In this section, we quickly cover the basics of sparse grids, following closely the recent work [36], to which we refer the reader for more details.

The sparse grid surrogate model, which in the following will be denoted by $S_f(\boldsymbol{p})$, can be informally described as an approximation of $f(\boldsymbol{p})$, obtained as a linear combination of several "small" tensor interpolants of f over Γ, denoted $f_{m(\boldsymbol{i})}(\boldsymbol{p})$ below, each formed by a limited number of points. The underlying idea is the so-called *sparsification principle*, i.e., the intuition that while none of these interpolants will be very accurate since they are all based on a few points, by carefully combining many of them one can recover an overall good surrogate model. This comes at a much lower cost than what would be needed if one were to build naively a tensor interpolant by covering the parameters space Γ with a tensorial Cartesian grid obtained by considering, say, M values for each parameter. Indeed, such an approach would involve a number of grid points exponential in the probabilistic dimension of the problems (M^N), i.e., it would be affected by the so-called *curse of dimensionality*, which makes the tensor product technique unfeasible, even for even moderately small N.

More precisely, the sparse grids surrogate model is expressed by means of the so-called *combination technique* formula

$$f(\boldsymbol{p}) \approx S_f(\boldsymbol{p}) = \sum_{\boldsymbol{i} \in \mathcal{I}} c_{\boldsymbol{i}} f_{m(\boldsymbol{i})}(\boldsymbol{p}), \quad c_{\boldsymbol{i}} = \sum_{\substack{\boldsymbol{j} \in \{0,1\}^N \\ \boldsymbol{i}+\boldsymbol{j} \in \mathcal{I}}} (-1)^{|\boldsymbol{j}|}, \tag{6}$$

where:

- $\boldsymbol{i} \in \mathbb{N}_+^N$ is a multi-index, i.e., a vector of N positive integer numbers; a tensor interpolant $f_{m(\boldsymbol{i})}(\boldsymbol{p})$ will be associated to each $\boldsymbol{i}$ in the set $\mathcal{I}$ (more on this later), and each entry i_k of $\boldsymbol{i}$ denotes the *level* of approximation of $f_{m(\boldsymbol{i})}(\boldsymbol{p})$ along each parameter $p_k, k = 1, \dots, N$;
- $m(\cdot)$ is an increasing function ("level-to-knots function"), such as $m(k) = k$ or $m(k) = 2^k$;
- $m(\boldsymbol{i})$ is the vector obtained applying $m(\cdot)$ to each component of $\boldsymbol{i}$, i.e., $m(\boldsymbol{i}) = [m(i_1), m(i_2), \dots]$;
- $f_{m(\boldsymbol{i})}(\boldsymbol{p})$ is a tensor interpolant, built over a Cartesian grid on Γ with $m(i_1) \times m(i_2) \times \dots$ points; more details on the construction and evaluation of $f_{m(\boldsymbol{i})}(\boldsymbol{p})$ are reported in Appendix B.
- $c_{\boldsymbol{i}}$ are the so-called *combination technique coefficients*. Note that some $c_{\boldsymbol{i}}$ might be null, in which case $f_{m(\boldsymbol{i})}(\boldsymbol{p})$ is not part of the final approximation;
- $\mathcal{I}$ is a multi-index set, $\mathcal{I} \subset \mathbb{N}_+^N$, that specifies which tensor interpolants are candidates to enter in the sparse grid construction. It should be chosen according to the sparsification principle mentioned above, and in particular, it should refrain from containing indices $\boldsymbol{i}$ whose entries are all large numbers (the cost of building the associated interpolant $f_{m(\boldsymbol{i})}(\boldsymbol{p})$ would be too large). Instead, whenever one entry (or a few entries) of $\boldsymbol{i}$ is large, the others should be kept as small as possible. Moreover, for technical reasons it is required that $\mathcal{I}$ is *downward-closed*, i.e., if $\boldsymbol{i} \in \mathcal{I}$ then all is "precedent" neighbors are also in $\mathcal{I}$.[1]

The set of points where $f(\boldsymbol{p})$ is evaluated (i.e., the union of all the points needed to assemble each $f_{m(\boldsymbol{p})}(\boldsymbol{p})$) is called *sparse grid*, and will be denoted by $\mathcal{G}$. Its cardinality will be denoted by G.

Eq. (6) becomes operative the moment we specify the three basic "ingredients" of the sparse grid construction, namely, the set $\mathcal{I}$, the function $m(\cdot)$ and the knots used to construct each tensor interpolant $f_{m(\boldsymbol{i})}(\boldsymbol{p})$. A lot of literature deals with criteria and algorithms to optimally choose these three components. In Section 4 we detail the choices we have adopted in this work. For examples of sparse grids in $N = 2$ dimensions we refer to Figs. 1(a) and 1(b).

3.3. Sparse grids for UQ

In this section, we provide an overview on how sparse grids can be used for UQ of a quantity of interest f. In our work, we have used the implementation of sparse grids provided in the Sparse Grids Matlab Kit (version 23-5 "Robert", see [36]), which can be used essentially "off-the-shelf" and renders these operations rather straightforward (this can be appreciated also by taking a look at the flow-chart depicted in Fig. 2 and Listings reported in Section 4).

[1] Upon denoting with $\boldsymbol{e}_k$ the kth versor of $\mathbb{N}^N$, i.e., the vector with all zeros expect the kth component, that is equal to 1, $\mathcal{I}$ is downward-closed if:

$$\boldsymbol{i} \in \mathcal{I} \Rightarrow \boldsymbol{i} - \boldsymbol{e}_k \in \mathcal{I}, \forall k = 1, \dots, N \text{ s.t. } i_k > 1.$$

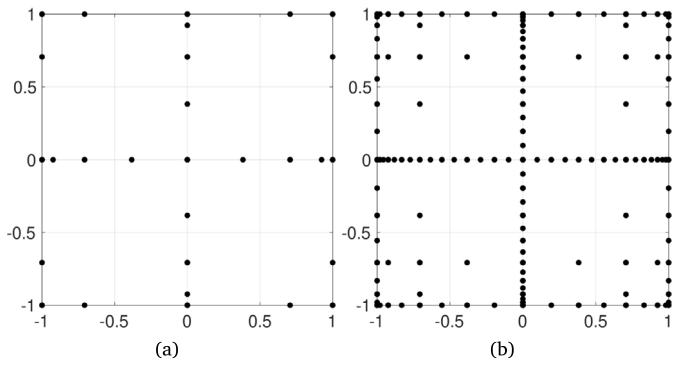

Fig. 1. Examples of sparse grids of level $w = 3$ (Fig. 1(a)) and level $w = 5$ (Fig. 1(b)) in $N = 2$ dimensions. We have used Clenshaw–Curtis points (8), function $m(\cdot)$ as in (9) and the multi-index set I as in (10).

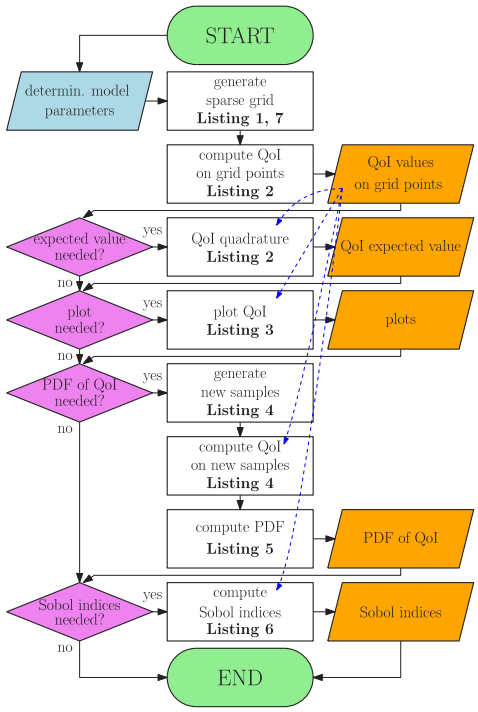

Fig. 2. Flow-chart of the algorithm. The dashed blue arrays indicate that the values of the QoI on the sparse grid points are needed for (i) using the sparse quadrature rule (7); (ii) plotting the QoI; (iii) evaluating the surrogate at new (i.e., non-grid) points; (iv) computing the Sobol indices.

Expected value. The univariate interpolation points used as basic blocks of the sparse grid construction are always associated with quadrature weights. For example, the weights corresponding to Clenshaw–Curtis points (used in our numerical experiments, see Section 4) can be computed by the Fast Fourier transform [43]. Recalling that expected values are just weighted integrals over Γ (cf. Eq. (5)), a *sparse grid quadrature* $Q[f]$ can be derived (mimicking the steps that would lead to Eq. (6)), which in practice simply amounts to taking weighted sums of the evaluations of f over the sparse grid points $\boldsymbol{q} \in \mathcal{G}$. The weights $\alpha_{\boldsymbol{q}}$ depend on the quadrature weights of the interpolation points and the combination technique coefficients c_i (see [36] for details):

$$\mathbb{E}[f] = \int_{\Gamma} f(\boldsymbol{p})\rho(\boldsymbol{p})d\boldsymbol{p} \approx \sum_{\boldsymbol{q}\in\mathcal{G}} \alpha_{\boldsymbol{q}} f(\boldsymbol{q}) = Q[f]. \tag{7}$$

See Listing 2 for software calls.

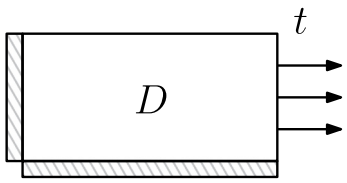

Fig. 3. Traction model. The external load is $\boldsymbol{t} = (1\,\mathrm{kN/m}, 0)^T$, homogeneous Neumann boundary conditions are imposed at the right and top part of the boundary, whereas the horizontal (vertical, respectively) displacement is imposed zero at the left (bottom, respectively) part of the boundary.

Variance and higher order indices. Simply employ the fact already recalled in Eq. (5) that $\mathbb{V}[f] = \mathbb{E}[f^2] - \mathbb{E}[f]^2$, and approximate both terms by sparse grids quadrature as explained above. Similar formulas exist for higher moments such as skewness (connected to $\mathbb{E}[f^3]$) and kurtosis (connected to $\mathbb{E}[f^4]$).

Global sensitivity analysis by Sobol indices. Sobol indices [44,45] are quantities that assess the contribution of each uncertain parameter to the total variance of a quantity of interest; the underlying mathematical machinery is a decomposition of the variance of f similar to the ANOVA decomposition. In particular, the *principal* Sobol index S_i^P quantifies the impact of each uncertain parameter p_i alone, whereas the *total* Sobol index S_i^T quantifies the impact of each uncertain parameter alone and in mixed effect with any other uncertain parameter. Principal and Sobol indices can be obtained by post-processing the sparse grid surrogate model $S_f(\boldsymbol{p})$, see [46] for details. See Listing 6 for implementation details.

Probability density function. An approximation of the pdf of f can be obtained by generating sufficiently many samples of the uncertain parameters $\boldsymbol{p}_i$ according to their pdf, evaluating f for each of them, and then resorting to binning algorithms to generate histograms of such values, or using functions such as kernel density estimates [47]. This process is significantly accelerated by replacing the values $f(\boldsymbol{p}_i)$ with their approximate counterparts $S_f(\boldsymbol{p}_i)$, [48]. To this end we remark that evaluating $S_f(\boldsymbol{p}_i)$ is essentially real-time (one only needs to evaluate a few polynomial interpolants), whereas evaluating $f(\boldsymbol{p}_i)$ requires solving a PDE (beam problem). See Listing 5 for implementation details.

4. Numerical experiments

All numerical tests deal with the traction problem (see Fig. 3), namely we take the external load $\boldsymbol{t} = (10^3\,\mathrm{kN/m}, 0)^T$ and impose the homogeneous Dirichlet boundary conditions on $\Sigma_s = [0, L]\times\{0\}\cup\{0\}\times[0, H]$ and homogeneous Neumann boundary conditions on $\partial D \setminus \Sigma_s$.

We now detail the choices adopted for the sparse grid construction illustrated in Section 3.2.

- As knots, we use the Clenshaw–Curtis points, which are well suited for uncertain parameters with uniform pdf.[2] A set of K points in $[-1, 1]$ can be computed as follows:

$$x_K^{(j)} = \cos\left(\frac{(j-1)\pi}{K-1}\right), \quad 1 \le j \le K, \tag{8}$$

and then if needed linearly transformed to any generic interval $[a, b]$.

[2] Note that equispaced points are in general *not* a good choice, due to the well-known Runge's phenomenon.

- As function $m(\cdot)$, we use the following

$$m(k) = \begin{cases} 1, & k = 1, \\ 2^{k-1} + 1, & k > 1 \end{cases} \tag{9}$$

which yields the doubling of the number of interpolation points, when moving from the interpolation level k to $k+1$. Note that this choice is particularly useful since it renders tensor interpolants built with Clenshaw–Curtis points *nested*, i.e., the set of points needed to build $f_{m(j)}(\boldsymbol{p})$ is contained in the set needed to build $f_{m(i)}(\boldsymbol{p})$ if the multi-indices $\boldsymbol{i} = (i_1, \dots, i_N)$ and $\boldsymbol{j} = (j_1, \dots, j_N)$ fulfill $j_k \le i_k$ for all $k = 1, \dots, N$. This property is clearly beneficial if one wants to refine a sparse grid already computed by adding further computations.

- As set $\mathcal{I}$ we use the classical choice

$$\mathcal{I} = \left\{ \boldsymbol{i} \in \mathbb{N}^N : \sum_{n=1}^{N} i_n \le w \right\}. \tag{10}$$

Note that, the larger w, the more points in the sparse grid. It is easy to see that it enforces a basic version of the sparsification principle; more sophisticated choices, such as anisotropic sets or adaptive algorithms for the selection of $\mathcal{I}$ are discussed, e.g., in [49–51] and [52,53], respectively.

Together, these three choices generate a sparse grid, which is commonly named in the literature as *Smolyak grid*.

In the following, we discuss two numerical examples with load and boundary conditions as in Fig. 3.

- In Section 4.1 we use three uncertain parameters to model the presence of one knot inside the unit square domain. The elasticity modulus fulfills the simplified assumption of being y-independent. We consider in this example two QoIs, namely (i) the entire displacement field and (ii) the horizontal displacement at the bottom-right corner of the domain. The outcomes are: (i) the numerical study of the approximation error of the first QoI; (ii) the construction of the surrogate for the second QoI, and the numerical study of its accuracy; (iii) pdf and Sobol indices of the second QoI.
- In Section 4.2 we consider a rectangular domain and use seven uncertain parameters to model the presence of two knots. In contrast to Section 4.1, here the elasticity modulus varies along both the horizontal and the vertical directions. Differently from before, in this example we consider only one QoI, i.e., the horizontal displacement at the bottom-right corner of the domain, and we compare two surrogates computed by means of Smolyak sparse grids and a-posteriori adaptive sparse grids, i.e., different strategies to compute the set $\mathcal{I}$.

4.1. One-knot example

In the first numerical example, we take $L = H = 1$ m and choose the stochastic elasticity modulus (2) depending on the uncertain vector $\boldsymbol{p} = (p_1, p_2, p_3)$ with length $N = 3$. More in details, we take $E_0 = 10^4$MPa and

$$\alpha(x, y, \boldsymbol{p}) = p_1 - \gamma \exp\left(-\frac{(x - p_2)^2}{2p_3^2} \right), \tag{11}$$

with $p_1 \sim \mathcal{U}(0.5, 1.5)$, $p_2 \sim \mathcal{U}(0.25, 0.75)$, $p_3 \sim \mathcal{U}(0.1, 0.2)$ and $\gamma = 0.4$.

Note that $\alpha(\cdot, \boldsymbol{p}) : D \to \mathbb{R}_+$ varies in the horizontal direction x, while it is constant in the vertical direction y. Therefore, the displacement along the vertical direction u_y is zero. This choice of α aims at modeling the presence of one knot along the beam. Following this interpretation, p_2 represents the (variable) center of the knot and p_3 represents its (variable) width; finally, $p_1 E_0$ is the (variable) nominal value of the Young modulus away from the knot. Note that the ranges of p_2 and p_3 are chosen so that the knot is well-contained inside the beam. We refer to Fig. 4(a), depicting a set of ten samples of E plotted versus the horizontal variable $x \in [0, 1]$, and Fig. 4(b), Fig. 4(c), where two samples of E are plotted versus $(x, y) \in D$. The IGA approximation of the corresponding solutions of problem (3) are shown in Fig. 4(e) and Fig. 4(f). For this numerical experiment, the IGA parameters are set to $r = q = 4$ and $N_{coll} = M_{coll} = 32$, leading to a negligible error in the space variables.

With the above-mentioned choices, the sparse grid of level w can be generated by running the very simple Matlab code in Listing 1.

4.1.1. QoI 1: Displacement field

The expected value of the solution $\boldsymbol{u}$ or a QoI of $\boldsymbol{u}$ can be computed by running the Matlab code in Listing 2. To this end, first the values of $\boldsymbol{u}$ (or $f(\boldsymbol{u})$) at all points of the sparse grid are computed (line 5), and then their weighted sum is calculated (line 6), cf Eq. (7). The brevity and simplicity of these listings testify how little extra work is needed to interface the beam solver to the UQ software, and thus how easy it is to perform a UQ analysis.

```
% number of parameters
N=3;
% knots for p1, p2 and p3
knots_p1=@(n) knots_CC(n,0.5,1.5,'prob');
knots_p2=@(n) knots_CC(n,0.25,0.75,'prob');
knots_p3=@(n) knots_CC(n,0.1,0.2,'prob');
knots = {knots_p1,knots_p2,knots_p3};
% functions m and t
[lev2knots,idxset]=define_functions_for_rule('SM',N)
% level
w = 1;
% sparse grid
S = create_sparse_grid(N,w,knots,lev2knots,idxset,[]);
% creates the "uniqued" list of points
Sr = reduce_sparse_grid(S)
```

Listing 1: Matlab code to create the Smolyak sparse grid.

```
% wrap the beam IGA solver into an @-function
f = @(y) solve_PDE(y);
% or further have the solver just return the QoI
% f = @(y) QoI(y);
f_values = evaluate_on_sparse_grids(f,Sr);
Eu = quadrature_on_sparse_grid(f_values,Sr);
%Eu = quadrature_on_sparse_grid(@(y)f(y),S,Sr);
```

Listing 2: Matlab code to compute the surrogate for the QoI.

In particular, we are interested in assessing the quality of the approximation of the expected value of the horizontal displacement field, i.e., of $\mathbb{E}[u_x]$, which we approximately obtained employing the Smolyak sparse grid of level $w = 7$ (see Fig. 4(d)). Coarser approximations of the expectation of the same quantity are then computed by Smolyak sparse grids of lower levels $w = 1, \dots, 5$. Their relative error with respect to the reference solution, measured in the $L^2(D)$-norm, is plotted in Fig. 5: the horizontal axis reports the cardinality of the employed sparse grid. For the sake of comparison, three instances of convergence of the Monte Carlo method are also depicted. When the sparse grid method is employed we observe an algebraic decay of the error with estimated slope -1.8, as opposed to the usual Monte Carlo decay rate $-1/2$ (i.e., the inverse of the square root of the number of Monte Carlo samples). We underline the effectiveness of the sparse grid approach, which delivers more accurate results with many less sample points than the plain Monte Carlo method.

```
% define range of the parameters
aa = [0.5, 0.25, 0.1];
bb = [1.5, 0.75, 0.2];
domain = [aa; bb];
```

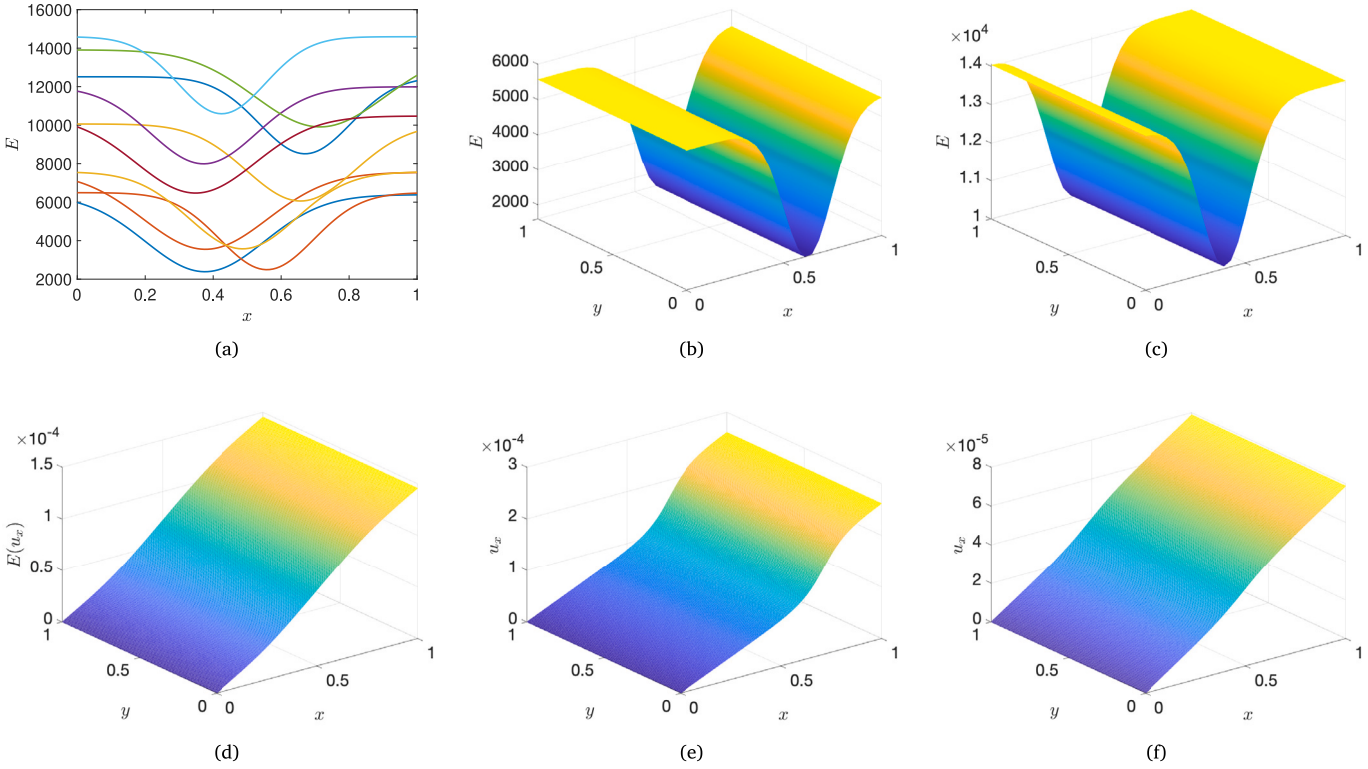

Fig. 4. 4(a) Ten samples of $E(x, \bar{y}, \boldsymbol{p})$, for fixed $\bar{y}$; 4(d) Reference solution for $\mathbb{E}[u_x]$ (Smolyak sparse grid surrogate of level $w = 7$); 4(b), 4(c) Plot of two samples of $E(x, y, \boldsymbol{p})$ as in (11) for $\boldsymbol{p} = (5567, 0.62277, 0.12425)$ and $\boldsymbol{p} = (14052, 0.39997, 0.11967)$, respectively; 4(e), 4(f) Plot of the two corresponding solutions $u_x(x, y, \boldsymbol{p})$ (3) ($\boldsymbol{p} = (5567, 0.62277, 0.12425)$ and $\boldsymbol{p} = (14052, 0.39997, 0.11967)$, respectively) computed via IGA (Section 2.2).

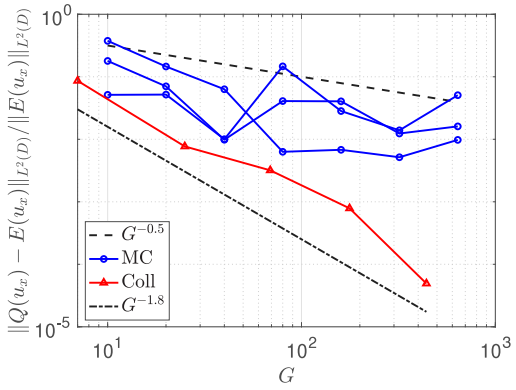

Fig. 5. Error convergence of the expected value of the horizontal displacement field in the $L^2(D)$-norm. The quantities are plotted versus the number of PDE solves (the cardinality G of the sparse grid for the Collocation method, the number of samples for the Monte Carlo method).

```
plot_sparse_grids_interpolant(S, Sr, domain, f_values,
    'with_f_values');
```

Listing 3: Matlab code to plot the sparse grid surrogate S_f.

4.1.2. QoI 2: Horizontal displacement at the bottom-right corner

Let us now consider the real-valued QoI being the evaluation of the horizontal displacement at the bottom-right corner of the beam, namely $f(\boldsymbol{p}) = u_x(1, 0, \boldsymbol{p})$. The surrogate of the QoI can be easily computed (see Listing 2) and plotted: see Listing 3 and Fig. 6(a), where level $w = 3$ is considered. In Fig. 6(b) we display a section of the three-dimensional plot in Fig. 6(a) obtained for the fixed value $p_2 = 0.25$. The plot shows that the variability of the QoI with respect to the parameters p_2 and p_3 is very limited. This observation will be confirmed later on, by means of the Sobol indices.

Table 1
Cardinality G of the employed sparse grids of increasing level w.

w	1	2	3	4	5
G	7	25	69	177	441

We now want to investigate the convergence of the sparse grid surrogate model, not only in the computation of the expected value, just like we did for the previous QoI, but also in point-wise prediction. Therefore, we generate $M = 2000$ new samples $\{\boldsymbol{p}^{(i)} = (p_1^{(i)}, p_2^{(i)}, p_3^{(i)}),\ i = 1, \dots, M\}$ of $\boldsymbol{p}$. For each of the new sample values, we compute the FOM solution and compare it with the evaluations of the Smolyak sparse grid surrogate S_f (see Listing 4). The relative error in the maximum norm is the given by

$$\left\| \frac{S_f - f}{f} \right\|_\infty = \max_{i=1,\dots,M} \left| \frac{S_f(\boldsymbol{p}^{(i)}) - f(\boldsymbol{p}^{(i)})}{f(\boldsymbol{p}^{(i)})} \right| \tag{12}$$

and is displayed in Fig. 7(b). For both the expected value and the point-wise prediction, an algebraic decay of the error is observed (with estimated rates of -2.7 and -2.5, respectively). Figs. 8(a) and 8(b) depict the scatterplot of the reference QoI (x-axis) and its surrogate (y-axis) of level $w = 2$ and $w = 3$, respectively, evaluated at the first 150 sample points $\boldsymbol{p}^{(i)}$ out of the 2000 samples just computed. As the level of the sparse grid increases, the blue dots tend to align along the bisector (red) line, reflecting better approximation properties of the surrogate.

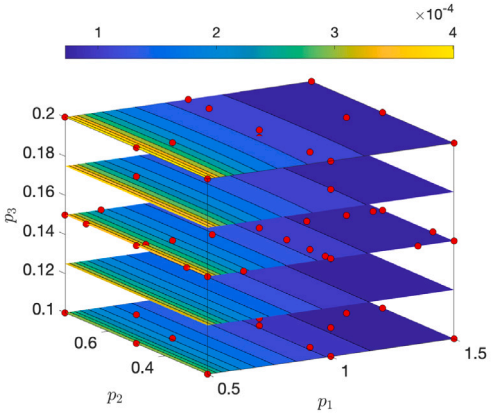

(a)

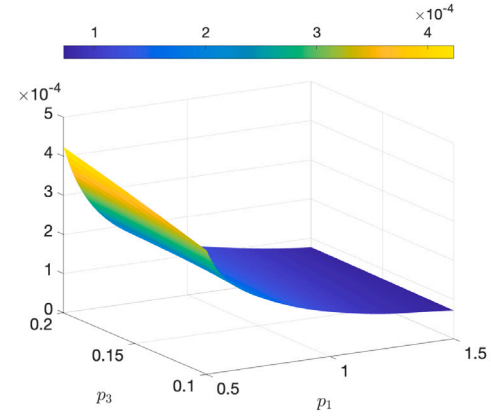

(b)

Fig. 6. 6(a) Three-dimensional plot of the surrogate QoI computed on the sparse grid with level $w = 3$; 6(b) Plot of the surrogate QoI versus p_1, p_3 and for fixed $p_2 = 0.25$.

Fig. 9 then graphically verifies the convergence of the pdf obtained by sampling the sparse grid surrogates $\mathcal{S}_f$, for increasing levels $w = 1, 2, 3$ (see Listing 5, where the built-in Matlab code `ksdensity` is used). For the level $w = 3$ we observe very good agreement between the reference curve and the surrogate one. Note that the alternative would be to compute the IGA solution collocated at all the $M = 2000$ samples $\{\boldsymbol{p}^{(i)}\}$, entailing a considerably larger computational effort.

We note that the computational cost required to construct the sparse grid surrogate $\mathcal{S}_f$ is given by $C \times G$, G being the cardinality of the sparse grid and C being the cost to solve one beam problem. Table 1 reports the size of all the sparse grids employed in the convergence plots, in correspondence with their level w. Instead, the computational cost required to compute the pdf is negligible.

```
% generate new samples of parameter values
p1 = rand(M,1)+0.5;
p2 = rand(M,1)*0.5 + 0.25;
p3 = rand(M,1)*0.1 + 0.1;
p = [p1, p2, p3];
% point_on_grid = evaluations of QoI on the points of
    Sr
point_surr = interpolate_on_sparse_grid(S,Sr,
    point_on_grid,p');
```

Listing 4: Matlab code to evaluate the surrogate at new parameter values.

```
% surrogate pdf for w=3 (use analogous code for w=1,2)
pdf = ksdensity(point_surr,'Support','positive');
```

Listing 5: Matlab code to compute the pdf obtained by sampling the sparse grid surrogate of the f.

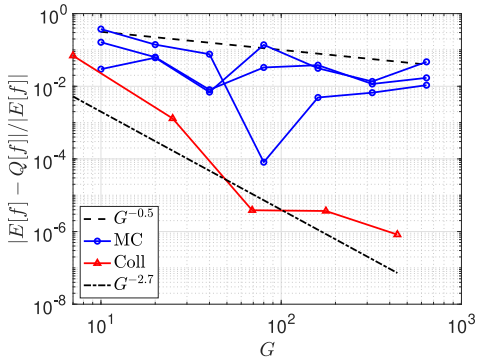

(a)

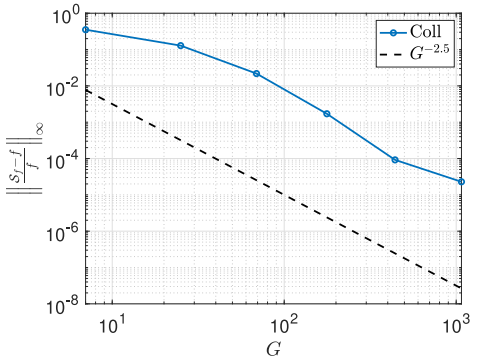

(b)

Fig. 7. 7(a) Relative error on the expectation of the QoI $f = u(1, 0, \cdot)$ plotted versus increasing cardinality G of sparse grids. For the sake of comparison, the Monte Carlo error is also depicted; 7(b) Maximum norm of the relative error on the QoI $f = u(1, 0, \cdot)$ plotted versus increasing cardinality G of sparse grids.

```
[Sob_princ,Sob_tot] =
    compute_sobol_indices_from_sparse_grid(S, Sr,
    f_values,domain,'legendre');
```

Listing 6: Matlab code to compute principal and total Sobol indices.

To conclude the UQ analysis, we compute the principal and total Sobol indices $\{S_i^P, i = 1, 2, 3\}$, $\{S_i^T, i = 1, 2, 3\}$ (see Section 3.3). They are computed according to Listing 6, the result being

$$S^P = [0.9818, 0.0000, 0.0088],$$
$$S^T = [0.9912, 0.0001, 0.0182].$$

They confirm that the variability of the second parameter p_2 does not affect the surrogate value, as previously observed by means of Fig. 6, and, moreover, they hint that the third parameter plays a negligible role as well.

As a conclusion of the analysis carried out, we can state that thanks to the sparse grid machinery, a small computational effort was enough to carry out a UQ analysis that allows us to draw these conclusions on the timber model at hand: (i) the parameter playing the most important role in the model is p_1; (ii) small variability of the QoI is caused by p_3; (iii) p_2 affects the QoI in a negligible way. These results are as expected, since p_2 and p_3 have local effects on the solution to the PDE (3), whereas the considered QoI is affected by global quantities, only.

4.2. Two-knots example

Let us take $L = 10$ m and $H = 1$ m, and choose

$$\alpha(x,y,\boldsymbol{p}) = p_1 - \gamma_1 \exp\left(-\frac{(x-\bar{x})^2}{2p_2^2}\right)\exp\left(-\frac{(y-\bar{y})^2}{2p_4^2}\right) - \gamma_2 \exp\left(-\frac{(x-\bar{x}-p_6)^2}{2p_3^2}\right)\exp\left(-\frac{(y-\bar{y}-p_7)^2}{2p_5^2}\right), \tag{13}$$

with parameter $\boldsymbol{p} = (p_1, p_2, p_3, p_4, p_5, p_6, p_7)$ whose entries are $p_1 \sim \mathcal{U}(0.5, 1.5)$, $p_2, p_3 \sim \mathcal{U}(0.3, 1)$, $p_4, p_5 \sim \mathcal{U}(0.03, 0.1)$, $p_6 \sim \mathcal{U}(1, 8)$ and $p_7 \sim \mathcal{U}(-0.5, 0.5)$, and with fixed values $\gamma_1 = \gamma_2 = 0.4$. In particular, in this second example, we aim to model the presence of two knots along the timber beam: one with fixed coordinates $(\bar{x}, \bar{y})$ and the second at random distance from the first one with coordinates $(\bar{x}+p_6, \bar{y}+p_7)$; the value of E_0 is again $E_0 = 10^4$ MPa. As in the first example, p_1 - when multiplied by E_0 - controls the nominal value of the Young modulus away from the knot. The remaining parameters model the width of the two knots along the horizontal (p_2, p_3) and vertical (p_4, p_5) directions. Fig. 10 depicts four samples of $E(x, y, \boldsymbol{p}) = E_0\alpha(x, y, \boldsymbol{p})$, with $\alpha(x, y, \boldsymbol{p})$ as in (13) (left column) and the first component of the corresponding IGA solution (right column). We underline that in the considered setting the second knot can be placed (i) close to the top/bottom boundary of the beam (first sample, showing the case of proximity to the top boundary); (ii) well-contained in the beam and distant from the first knot (second sample); (iii) well contained in the beam but close to the first knot (third sample); (iv) close to the right boundary of the beam (fourth sample).

In this second example, we are dealing with a problem with a larger number of uncertain parameters, therefore we consider not only the classical Smolyak sparse grids used in the previous example, but also the more effective a-posteriori adaptive sparse grids. In this version of sparse grids, multi-indices $\boldsymbol{i}$ are added to the multi-index set $\mathcal{I}$ in Eq. (6) in an iterative way, following a simple yet powerful procedure based on an error-cost criterion (see e.g., [52,53] for details):

- a number of potential candidates $\boldsymbol{j}$ is added to the sparse grid to the multi-index set $\mathcal{I}$;
- for each of them a profit indicator is computed (i.e., the ratio between the change in the prediction of $\mathbb{E}[f]$ due to having added $\boldsymbol{j}$ to the sparse grid and the number of new FOM evaluations requested by it);
- the candidate with the largest profit is selected and added to $\mathcal{I}$, and the set of candidates is updated accordingly.

This algorithm is usually very effective in quickly determining a good set $\mathcal{I}$, although it is not entirely optimal in terms of cost since the profits are evaluated only *after* having performed the corresponding FOM evaluations (hence the name "a-posteriori adaptive"), therefore some computational cost is "wasted" to detect multi-indices with small profit.

Returning to the computational example, let us consider the same real-valued QoI as in the first example, namely, the evaluation of the horizontal displacement at the bottom-right corner of the beam $f(\boldsymbol{p}) = u_x(10, 0, \boldsymbol{p})$. The reference value $\mathbb{E}[u_x(10, 0, \cdot)]$ is approximated using an a-posteriori adaptive sparse grid with 30105 collocation points (see Listing 7) and is compared with its approximation $\mathcal{Q}[u_x(10, 0, \cdot)]$ computed either using Smolyak sparse grids of increasing level $w = 1, \ldots, 6$ (red line in Fig. 11) or a-posteriori adaptive sparse grids with increasing number of collocation points (magenta line in Fig. 11). Table 2 reports the cardinality of the Smolyak sparse grids of increasing level w.

Following the same lead as in the first example, we now want to investigate the convergence of the sparse grid surrogate to the FOM. Therefore, the QoI is computed by the FOM in $M = 5000$ randomly generated samples of $\boldsymbol{p}$ (denoted as $\{\boldsymbol{p}^{(i)}, i = 1, \ldots, M\}$). In contrast, the a-posteriori adaptive and the Smolyak sparse grid surrogates are evaluated at all points $\boldsymbol{p}^{(i)}$ and the largest relative error is computed by Eq. (12). The decay of this approximation error as the sparse grids construction cost increases is depicted in Fig. 12. Both Figs. 11 and 12 display improved rates of convergence of the a-posteriori adaptive sparse grids, when compared to the non-adaptive ones (i.e., the Smolyak sparse grids).

Table 2
Cardinality G of the employed Smolyak sparse grids of increasing level w.

w	1	2	3	4	5
G	15	113	589	2465	9017

Next, we graphically verify the convergence of the pdf obtained by sampling the a-posteriori adaptive sparse grid surrogate, see Fig. 13: a very good agreement between the exact and the surrogate pdfs can be observed. Finally, the principal and total Sobol indices are computed:

$$S^P = [0.9914, 0.0000, 0.0040, 0.0001, 0.0001, 0.0002, 0.0002],$$
$$S^T = [0.9945, 0.0002, 0.0075, 0.0002, 0.0008, 0.0003, 0.0010].$$

As observed in the first example, the first parameter p_1 is by far the most important, in the sense that it essentially affects all the variability of the selected QoI. The other parameters play a much smaller role, and in particular the second p_2 (horizontal width of the first knot) appears to be negligible.

```
% number of parameters
N=7;
% knots for p1, p2, p3, p4, p5, p6 and p7
knots_Y0=@(n) knots_CC(n,0.5,1.5,'prob'); % c
knots_Y1=@(n) knots_CC(n,1,8,'prob'); % r
knots_Y2=@(n) knots_CC(n,-0.5,0.5,'prob'); % s
knots_Y3=@(n) knots_CC(n,0.3,1,'prob'); % sx1
knots_Y4=@(n) knots_CC(n,0.3,1,'prob'); % sx2
knots_Y5=@(n) knots_CC(n,0.03,0.1,'prob'); % sy1
knots_Y6=@(n) knots_CC(n,0.03,0.1,'prob'); % sy2
knots = {knots_Y0,knots_Y1,knots_Y2,knots_Y3,knots_Y4,
    knots_Y5,knots_Y6};
lev2knots = @lev2knots_nested
% number of maximum collocation points
Max_Points = 30000;
controls.max_pts=Max_Points;
% QoI (to be implemented separately)
f = @(y) QoI(y);
adapt = adapt_sparse_grid(f,N,knots,lev2knots,[],
    controls)
```

Listing 7: Matlab code to compute an adaptive sparse grid approximation of the QoI.

5. Conclusions

In this paper, we used the Sparse Grid Matlab kit (freely available online) for the UQ of the displacements in the field of continuum linear mechanics. The considered problem has been discretized by means of the IGA collocation (in the space variables), while the dependence on random parameters has been treated by means of the stochastic collocation method on both Smolyak and a-posteriori adaptive sparse grids.

The use of the Sparse Grid Matlab kit presents several advantages. First, it can be easily interfaced with any black-box solver for the (deterministic) mechanical problem. Second, the numerical methods implemented in the kit outperform standard UQ techniques, such as the plain Monte Carlo method. Finally, it provides outputs that can be readily interpreted and exploited in the engineering practice.

In this work, we treated linear-elastic, isotropic material. However, due to the black-box nature of sparse grids, any non-linearity can be

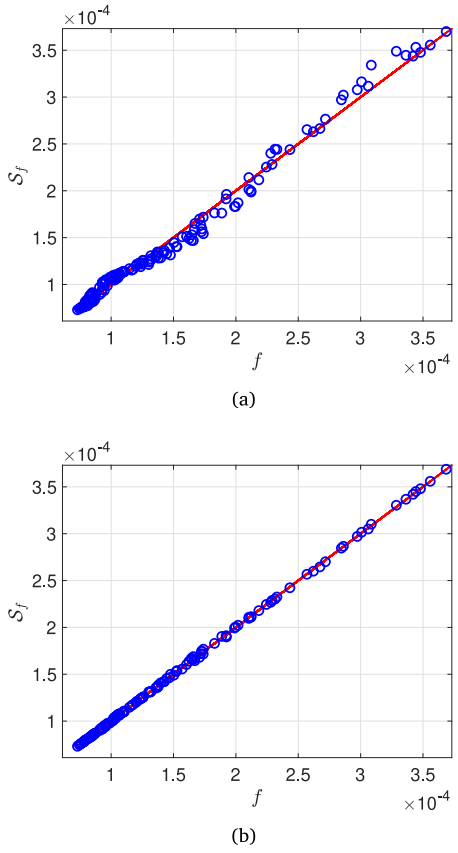

Fig. 8. Scatterplot of the reference QoI (x-axis) and the surrogate QoI (y-axis) of level $w = 2$ (Fig. 8(a)) and level $w = 3$ (Fig. 8(b)) evaluated at the first 150 sample points $\boldsymbol{p}^{(i)}$. The bisector line is depicted in red.

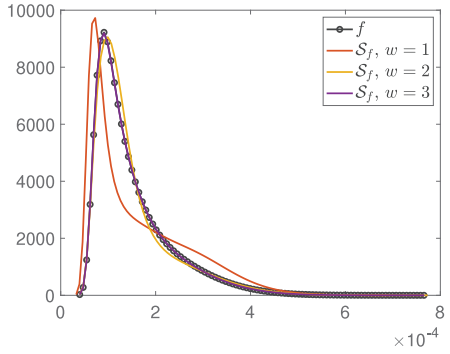

Fig. 9. Approximations to the pdf of the considered f for increasing levels of sparse grids. The reference pdf is computed starting from evaluations of the FOM.

easily included, just replacing IGA collocation with a suitable numerical implementation of non-linear Partial Differential Equations (PDEs). Future work will include the analysis of more sophisticated and possibly anisotropic and non-linear mechanical problems, where the variability of grain direction is accounted for and modeled as a more complex random field.

CRediT authorship contribution statement

Giuseppe Balduzzi: Conceptualization, Investigation, Methodology, Software, Writing – original draft, Writing – review & editing. **Francesca Bonizzoni:** Conceptualization, Investigation, Methodology, Writing – original draft, Software, Writing – review & editing. **Lorenzo Tamellini:** Conceptualization, Investigation, Methodology, Software, Writing – original draft, Writing – review & editing.

Declaration of competing interest

The authors declare that they have no known competing financial interests or personal relationships that could have appeared to influence the work reported in this paper.

Data availability

No data was used for the research described in the article.

Acknowledgments

Lorenzo Tamellini has been supported by the PRIN 2017 project 201752HKH8 "Numerical Analysis for Full and Reduced Order Methods for the efficient and accurate solution of complex systems governed by Partial Differential Equations (NA-FROM-PDEs)". Lorenzo Tamellini also acknowledges the support of GNCS-INdAM (Gruppo Nazionale Calcolo Scientifico - Istituto Nazionale di Alta Matematica), Italy. F. Bonizzoni is member of the INdAM Research group GNCS and her work was part of a project that has received funding from the European Research Council ERC under the European Union's Horizon 2020 research and innovation program (Grant agreement No. 865751 – RandomMultiScales). Finally, the authors would like to acknowledge Alessandro Reali for his contribution in the development of the IGA collocation code.

Appendix A. Basics on B-splines

Let us introduce two knot vectors:

$$X = \{x_1 = 0 \le x_1 \le \cdots \le x_{N_{coll}+r+1} = L\}$$
$$Y = \{y_1 = 0 \le y_1 \le \cdots \le y_{M_{coll}+q+1} = H\} \tag{A.1}$$

where r and q are the degree of the B-splines and N_{coll} and M_{coll} are the numbers of basis functions. Pairs $(x_i, y_j) \in X \times Y$ correspond to coordinates of points in the 2D domain D. In particular, we take X, Y as so-called *open* vectors, i.e., the first and last knots of X (Y, respectively) have multiplicity $r + 1$ ($q + 1$, respectively), and – for simplicity – we choose uniformly equispaced X and Y knots.

Given the knot vector X, the uni-variate B-spline basis functions in the x-variable are defined recursively as follows:

- for $r = 0$:

$$N_i^0(x) = \begin{cases} 1, & \text{if } x_i \le x < x_{i+1}, \\ 0, & \text{otherwise,} \end{cases}$$

- for $r > 1$:

$$N_i^r(x) = \begin{cases} \frac{x - x_i}{x_{i+r} - x_i} N_{i,r-1}(x) + \frac{x_{i+r+1} - x}{x_{i+r+1} - x_{i+1}} N_{i+1,r-1}(x), \\ \text{if } x_i \le x < x_{i+r+1}, \\ 0, \text{ otherwise,} \end{cases}$$

with the convention $0/0 = 0$. Given the knot vector Y, the uni-variate B-spline basis functions $M_j^q(y)$ are defined analogously. The tensor product construction leads to bi-variate basis functions for the 2D domain D, given by

$$R_{i,j}^{r,q}(x, y) = N_i^r(x)\, M_j^q(y)$$

for all $i = 1, \ldots, N_{coll}$, $j = 1, \ldots, M_{coll}$.

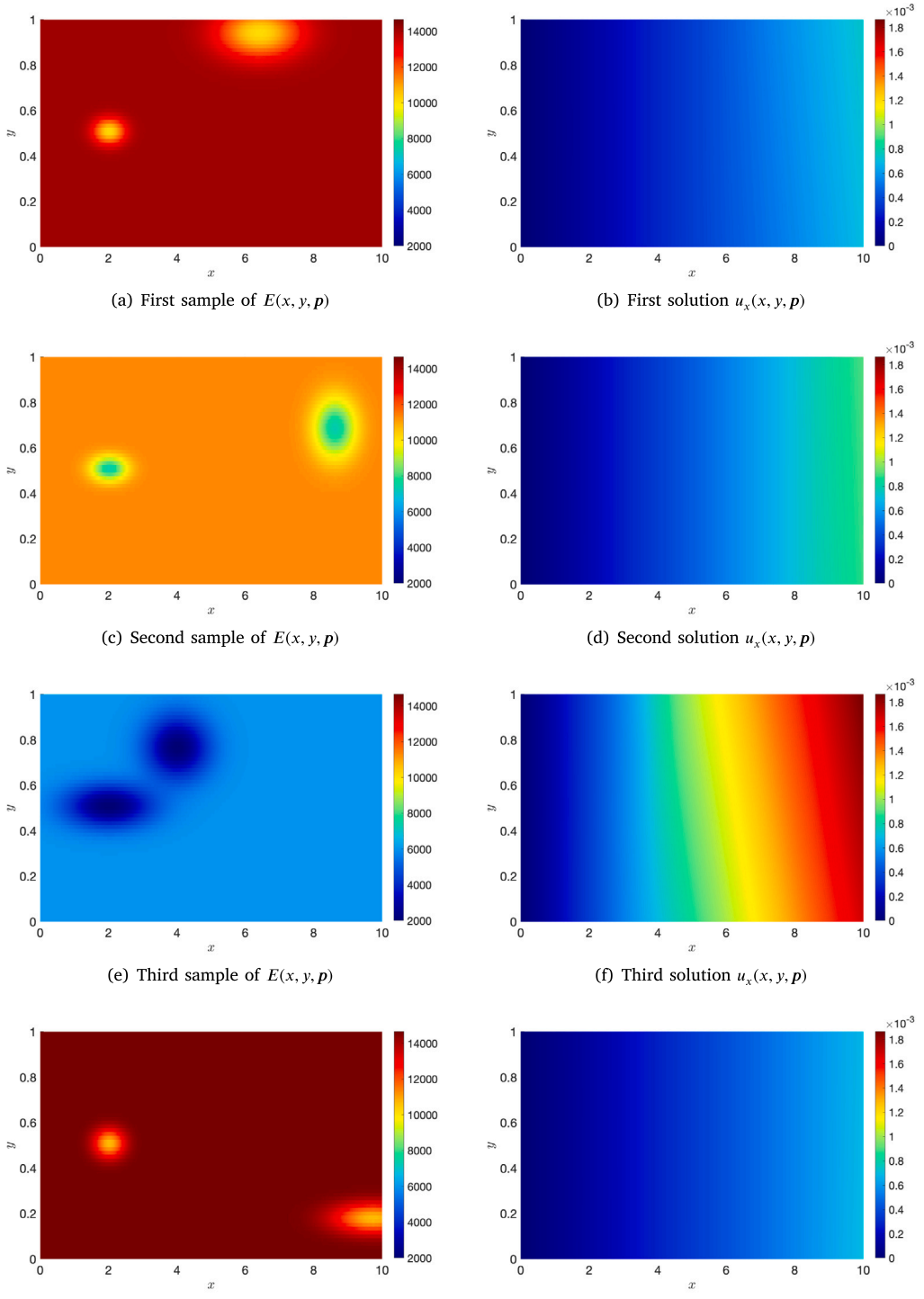

(a) First sample of $E(x, y, \boldsymbol{p})$ (b) First solution $u_x(x, y, \boldsymbol{p})$

(c) Second sample of $E(x, y, \boldsymbol{p})$ (d) Second solution $u_x(x, y, \boldsymbol{p})$

(e) Third sample of $E(x, y, \boldsymbol{p})$ (f) Third solution $u_x(x, y, \boldsymbol{p})$

(g) Fourth sample of $E(x, y, \boldsymbol{p})$ (h) Fourth solution $u_x(x, y, \boldsymbol{p})$

Fig. 10. Plot of four samples of $E(x, y, \boldsymbol{p}) = E_0\alpha(x, y, \boldsymbol{p})$, with $\alpha(x, y, \boldsymbol{p})$ as in (13) and of the corresponding horizontal displacement $u_x(x, y, \boldsymbol{p})$ computed via the IGA method (Section 2.2) for $\boldsymbol{p} = (14134, 4.3976, 0.4340, 0.3323, 0.8566, 0.0414, 0.0789)$, $\boldsymbol{p} = (11324, 6.6020, 0.1787, 0.3680, 0.4308, 0.0383, 0.0924)$, $\boldsymbol{p} = (5.9754, 1.9932, 0.2577, 0.8764, 0.6428, 0.0649, 0.0972)$ and $\boldsymbol{p} = (1.4649, 7.7164, -0.3288, 0.3241, 0.8283, 0.0457, 0.0480)$ (from top to bottom).

Appendix B. Formulas for sparse grids

In this appendix, we report some auxiliary formulas for readers who are interested in the details of how the tensor interpolant $f_{m(\boldsymbol{i})}$ in Eq. (6) is obtained. To this end, let us recall that $\boldsymbol{i}$ is a vector of N positive integers, and that $m(\cdot)$ is an increasing function. We then let:

- $\mathcal{G}_{n,m(i_n)}$ a set of $m(i_n)$ points in the range of the nth parameter p_n, (for instance, the Clenshaw–Curtis points introduced in Eq. (8)),

$$\mathcal{G}_{n,m(i_n)} = \{p^1_{n,m(i_n)}, p^2_{n,m(i_n)}, \dots, p^{m(i_n)}_{n,m(i_n)}\}$$

- $\ell^k_{n,m(i_n)}$ be the Lagrange polynomial associated to the kth node of $\mathcal{G}_{n,m(i_n)}$, i.e., a polynomial that has value 1 in $p^k_{n,m(i_n)}$ and 0 in every

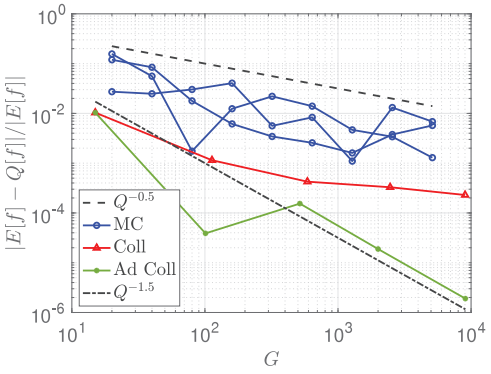

Fig. 11. Error convergence of the sparse grid surrogates. As a comparison, three instances of Monte Carlo errors are also reported. The lines are plotted versus the number of PDE solves (the cardinality G of the sparse grid the Collocation method, the number of samples for the Monte Carlo method).

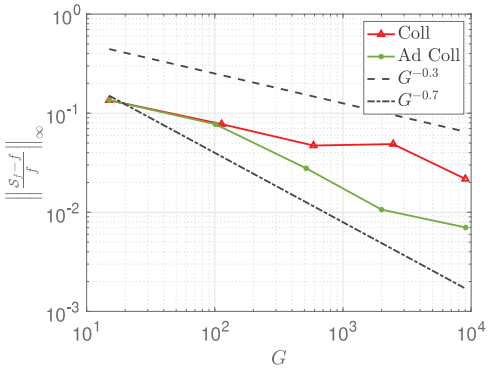

Fig. 12. Maximum norm of the relative error on the QoI $f = u_x(10, 0, \cdot)$ plotted versus increasing cardinality of sparse grids.

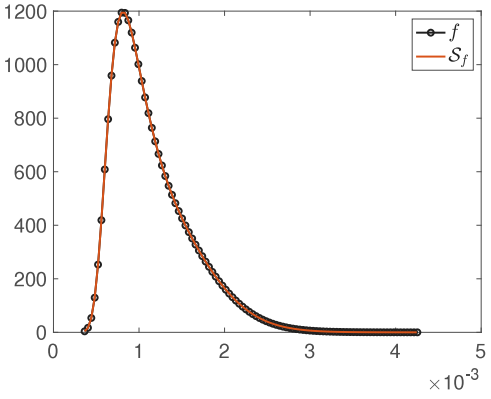

Fig. 13. Approximation to the pdf of the considered f corresponding to the surrogate obtained by means of the a-posteriori adaptive sparse grid. The reference pdf is computed starting from evaluations of the FOM.

other point of $\mathcal{G}_{n,m(i_n)}$. The explicit expression of $\ell^k_{n,m(i_n)}(p)$ reads:

$$\ell^k_{n,m(i_n)}(p) = \prod_{j=1, j\neq k}^{m(i_n)} \frac{p - p^j_{n,m(i_n)}}{p^k_{n,m(i_n)} - p^j_{n,m(i_n)}}.$$

- $\mathcal{G}_{m(\boldsymbol{i})}$ is the cartesian product of the univariate sets $\mathcal{G}_{n,m(i_n)}$, for $n = 1, \ldots, N$, namely

$$\mathcal{G}_{m(\boldsymbol{i})} = \prod_{n=1}^{N} \mathcal{G}_{n,m(i_n)}.$$

It contains $m(i_1) \times m(i_2) \times \cdot m(i_N)$ points. Each of these points corresponds a multi-index $\boldsymbol{j}$, that is component-wise smaller than $m(\boldsymbol{i})$, i.e.,

$$\mathcal{G}_{m(\boldsymbol{i})} = \{\boldsymbol{p}_{\boldsymbol{j}} \in \mathbb{R}^N : p_{j_n} = x^{j_n}_{n,m(i_n)} \text{with } j_n \leq m(i_n)\}.$$

- To each $\boldsymbol{p}_{\boldsymbol{j}}$ we can associate the multi-variate Lagrange polynomial given by

$$\ell^{\boldsymbol{j}}_{m(\boldsymbol{i})}(\boldsymbol{p}) = \prod_{n=1}^{N} \ell^{j_n}_{n,m(i_n)}(p_n).$$

With these definitions in place, we can finally define the tensor interpolant $f_{m(\boldsymbol{i})}$ as

$$f_{m(\boldsymbol{i})}(\boldsymbol{p}) = \sum_{\boldsymbol{p}_{\boldsymbol{j}} \in \mathcal{G}_{m(\boldsymbol{i})}} f(\boldsymbol{p}_{\boldsymbol{j}}) \ell^{\boldsymbol{j}}_{m(\boldsymbol{i})}(\boldsymbol{p}).$$

The sparse grid $\mathcal{G}$ (i.e., the union of the points required to assemble each $f_{m(\boldsymbol{i})}$ in Eq. (6)) can be obtained as

$$\mathcal{G} = \bigcup_{\boldsymbol{i} \in \mathcal{I}} \mathcal{G}_{m(\boldsymbol{i})}.$$

References

[1] I. Smith, M.A. Snow, Timber: An ancient construction material with a bright future, For. Chron. 84 (4) (2008) 504–510.

[2] A. Ngowi, E. Pienaar, A. Talukhaba, J. Mbachu, The globalisation of the construction industry—a review, Buil. environ. 40 (1) (2005) 135–141.

[3] Z. Xing, J. Wang, J. Zhang, Expansion of environmental impact assessment for eco-efficiency evaluation of China's economic sectors: An economic input–output based frontier approach, Sci. Total Environ. 635 (2018) 284–293.

[4] A. Tukker, B. Jansen, Environmental impacts of products: A detailed review of studies, J. Ind. Ecol. 10 (3) (2006) 159–182.

[5] T. Singh, D. Page, I. Simpson, Manufactured structural timber building materials and their durability, Constr. Build. Mater. 217 (2019) 84–92.

[6] M. Autengruber, M. Lukacevic, C. Gröstlinger, J. Füssl, Finite-element-based prediction of moisture-induced crack patterns for cross sections of solid wood and glued laminated timber exposed to a realistic climate condition, Constr. Build. Mater. 271 (2021) 121775.

[7] Y. Li, B.Y. Lattimer, S.W. Case, Measurement and modelling of thermal and physical properties of wood construction materials, Constr. Build. Mater. 284 (2021) 122780.

[8] H.J. Blaß, C. Sandhaas, Timber Engineering-Principles for Design, KIT Scientific Publishing, 2017.

[9] C. Goldhahn, E. Cabane, M. Chanana, Sustainability in wood materials science: An opinion about current material development techniques and the end of lifetime perspectives, Phil. Trans. R. Soc. A 379 (2206) (2021) 20200339.

[10] L. Gustavsson, R. Sathre, Energy and CO2 analysis of wood substitution in construction, Clim. Change 105 (1) (2011) 129–153.

[11] C. Vida, M. Lukacevic, J. Eberhardsteiner, J. Füssl, Modeling approach to estimate the bending strength and failure mechanisms of glued laminated timber beams, Eng. Struct. 255 (2022) 113862.

[12] H. Petersson, Use of optical and laser scanning techniques as tools for obtaining improved FE-input data for strength and shape stability analysis of wood and timber, in: ECCM, 2010, 2010, Full–paper.

[13] F. Longuetaud, F. Mothe, B. Kerautret, A. Krähenbühl, L. Hory, J.M. Leban, I. Debled-Rennesson, Automatic knot detection and measurements from X-ray CT images of wood: A review and validation of an improved algorithm on softwood samples, Comput. Electron. Agric. 85 (2012) 77–89.

[14] G. Kandler, M. Lukacevic, J. Füssl, An algorithm for the geometric reconstruction of knots within timber boards based on fibre angle measurements, Constr. Build. Mater. 124 (2016) 945–960.

[15] M. Lukacevic, G. Kandler, M. Hu, A. Olsson, J. Füssl, A 3D model for knots and related fiber deviations in sawn timber for prediction of mechanical properties of boards, Mater. Des. 166 (2019) 107617.

[16] S. Sahu, P. Sarkar, R. Davis, Quantification of uncertainty in compressive strength of fly ash brick masonry, J. Build. Eng. 26 (2019) 100843.

[17] L. De Simon, M. Iglesias, B. Jones, C. Wood, Quantifying uncertainty in thermophysical properties of walls by means of Bayesian inversion, Energy Build. 177 (2018) 220–245.

[18] C. Jenkel, F. Leichsenring, W. Graf, M. Kaliske, Stochastic modelling of uncertainty in timber engineering, Eng. Struct. 99 (2015) 296–310.

[19] S. Gonen, B. Pulatsu, E. Erdogmus, P.B. Lourenço, S. Soyoz, Effects of spatial variability and correlation in stochastic discontinuum analysis of unreinforced masonry walls, Constr. Build. Mater. 337 (2022) 127511.

[20] S. Gonen, B. Pulatsu, P.B. Lourenço, J.V. Lemos, K. Tuncay, E. Erduran, Analysis and prediction of masonry wallette strength under combined compression-bending via stochastic computational modeling, Eng. Struct. 278 (2023) 115492.
[21] G. Kandler, J. Füssl, J. Eberhardsteiner, Stochastic finite element approaches for wood-based products: Theoretical framework and review of methods, Wood Sci. Technol. 49 (5) (2015) 1055–1097.
[22] J. Füssl, G. Kandler, J. Eberhardsteiner, Application of stochastic finite element approaches to wood-based products, Arch. Appl. Mech. 86 (1–2) (2016) 89–110.
[23] G. Kandler, J. Füssl, A probabilistic approach for the linear behaviour of glued laminated timber, Eng. Struct. 148 (2017) 673–685.
[24] C. Czech, F. Seeber, A. Khaloian Sarnaghi, F. Duddeck, Quantification of spatial inhomogeneous material properties: Wooden laser scanned fibre deviations modelled by Gaussian processes, in: 8th European Congress on Computational Methods in Applied Sciences and Engineering, 2022.
[25] A.I.B. Farouk, J. Zhu, J. Ding, S. Haruna, Prediction and uncertainty quantification of ultimate bond strength between UHPC and reinforcing steel bar using a hybrid machine learning approach, Constr. Build. Mater. 345 (2022) 128360.
[26] M.S.T. Nguyen, S.-E. Kim, A hybrid machine learning approach in prediction and uncertainty quantification of ultimate compressive strength of RCFST columns, Constr. Build. Mater. 302 (2021) 124208.
[27] O. Le Maître, O.M. Knio, Spectral Methods for Uncertainty Quantification: with Applications to Computational Fluid Dynamics, Springer Science & Business Media, 2010.
[28] Martin Eigel, Claude Jeffrey Gittelson, Christoph Schwab, Elmar Zander, A convergent adaptive stochastic Galerkin finite element method with quasi-optimal spatial meshes, in: ESAIM: M2AN, 49 (5) (2015) 1367–1398.
[29] F. Bonizzoni, F. Nobile, Regularity and sparse approximation of the recursive first moment equations for the lognormal Darcy problem, Comput. Math. Appl. 80 (12) (2020) 2925–2947.
[30] F. Bonizzoni, F. Nobile, D. Kressner, Tensor train approximation of moment equations for elliptic equations with lognormal coefficient, Comput. Methods Appl. Mech. Engrg. 308 (2016) 349–376.
[31] F. Bonizzoni, F. Nobile, Perturbation analysis for the Darcy problem with log-normal permeability, SIAM/ASA J. Uncertain. Quantif. 2 (1) (2014) 223–244.
[32] F. Bonizzoni, A. Buffa, F. Nobile, Moment equations for the mixed formulation of the hodge Laplacian with stochastic loading term, IMA J. Numer. Anal. 34 (4) (2013) 1328–1360.
[33] C.E. Rasmussen, C.K.I. Williams, Gaussian Processes for Machine Learning, MIT Press, 2006.
[34] I. Babuška, F. Nobile, R. Tempone, A stochastic collocation method for elliptic partial differential equations with random input data, SIAM Rev. 52 (2) (2010) 317–355.
[35] D. Xiu, J. Hesthaven, High-order collocation methods for differential equations with random inputs, SIAM J. Sci. Comput. 27 (3) (2005) 1118–1139.
[36] C. Piazzola, L. Tamellini, The sparse grids matlab kit - a Matlab implementation of sparse grids for high-dimensional function approximation and uncertainty quantification, 2022, ArXiv - (2203.09314).
[37] Chen P., Sparse quadrature for high-dimensional integration with Gaussian measure, ESAIM: M2AN 52 (2) (2018) 631–657.
[38] O.G. Ernst, B. Sprungk, L. Tamellini, Convergence of sparse collocation for functions of countably many Gaussian random variables (with application to lognormal elliptic diffusion problems), SIAM J. Num. Anal. 56 (2) (2018) 877–905.
[39] F. Auricchio, L.B. Da Veiga, T.J. Hughes, A. Reali, G. Sangalli, Isogeometric collocation for elastostatics and explicit dynamics, Comput. Methods Appl. Mech. Engrg. 249 (2012) 2–14.
[40] R.B. Nelsen, An Introduction to Copulas, Springer New York, 2007.
[41] R. Ghanem, D. Higdon, H. Owhadi, Handbook of Uncertainty Quantification, Handbook of Uncertainty Quantification, Springer International Publishing, 2016.
[42] G. Kandler, M. Lukacevic, C. Zechmeister, S. Wolff, J. Füssl, Stochastic engineering framework for timber structural elements and its application to glued laminated timber beams, Constr. Build. Mater. 190 (2018) 573–592.
[43] L.N. Trefethen, Is Gauss quadrature better than Clenshaw-Curtis? SIAM Rev. 50 (1) (2008) 67–87.
[44] B. Sudret, Global sensitivity analysis using polynomial chaos expansions, Reliab. Eng. Syst. Saf. 93 (7) (2008) 964–979.
[45] G.E.B. Archer, A. Saltelli, I.M. Sobol, Sensitivity measures, anova-like techniques and the use of bootstrap, J. Stat. Comput. Simul. 58 (2) (1997) 99–120.
[46] L. Formaggia, A. Guadagnini, I. Imperiali, V. Lever, G. Porta, M. Riva, A. Scotti, L. Tamellini, Global sensitivity analysis through polynomial chaos expansion of a basin-scale geochemical compaction model, Comput. Geosci. 17 (1) (2013) 25–42.
[47] M. Rosenblatt, Remarks on some nonparametric estimates of a density function, Ann. Math. Stat. 27 (3) (1956) 832–837.
[48] A. Sagiv, Spectral convergence of probability densities for forward problems in uncertainty quantification, Numer. Math. 150 (4) (2022) 1165–1186.
[49] F. Nobile, R. Tempone, C. Webster, An anisotropic sparse grid stochastic collocation method for partial differential equations with random input data, SIAM J. Numer. Anal. 46 (5) (2008) 2411–2442.
[50] A. Chkifa, A. Cohen, C. Schwab, High-dimensional adaptive sparse polynomial interpolation and applications to parametric PDEs, Found. Comput. Math. (2013) 1–33.
[51] F. Nobile, L. Tamellini, R. Tempone, Convergence of quasi-optimal sparse-grid approximation of Hilbert-space-valued functions: Application to random elliptic PDEs, Numerische Math. 134 (2) (2016) 343–388.
[52] T. Gerstner, M. Griebel, Dimension-adaptive tensor-product quadrature, Computing 71 (1) (2003) 65–87.
[53] F. Nobile, L. Tamellini, F. Tesei, R. Tempone, An adaptive sparse grid algorithm for elliptic PDEs with lognormal diffusion coefficient, in: J. Garcke, D. Pflüger (Eds.), Sparse Grids and Applications – Stuttgart 2014, in: Vol. 109 of Lecture Notes in Computational Science and Engineering, Springer International Publishing Switzerland, 2016, pp. 191–220.